PHYSICAL REVIEW B **85**, 245118 (2012)

Internal electric fields and color shift in Cr^{3+}-based gemstones

J. A. Aramburu,[1] P. Garcia-Fernandez,[1] J. M. García-Lastra,[2] M. T. Barriuso,[3] and M. Moreno[1]
[1]*Departamento de Ciencias de la Tierra y Física de la Materia Condensada, Universidad de Cantabria, Avenida de los Castros s/n, 39005 Santander, Spain*
[2]*Center for Atomic-Scale Materials Design, Department of Physics, Technical University of Denmark, DK-2800 Kongens Lyngby, Denmark*
[3]*Departamento de Física Moderna, Universidad de Cantabria, Avenida de los Castros s/n, 39005 Santander, Spain*

(Received 16 February 2012; published 18 June 2012)

Seeking to better understand the origin of the different colors of emerald and ruby, both *ab initio* periodic and cluster calculations have been carried out. The calculations reproduce the interatomic distances measured for pure $Be_3Si_6Al_2O_{18}$ and Al_2O_3 as well as the $Cr^{3+}-O^{2-}$ distances in emerald and ruby. The mean $Cr^{3+}-O^{2-}$ distance for $Be_3Si_6Al_2O_{18}$:Cr^{3+} and Al_2O_3:Cr^{3+} is found to be practically equal to 1.97 Å, in agreement with recent experimental values. The present calculations confirm that the variations of optical properties due to Cr^{3+} impurities along the series of ionic oxides can be understood merely through the ${CrO_6}^{9-}$ unit but subject to the electric field due to the rest of the lattice ions. As a salient feature it is proved that changes in electronic density and covalency due to the internal field are not the cause of the color shift. Therefore, the red color of ruby is not due to the polarization of the electronic cloud around chromium as a result of the C_3 local symmetry. The present study also demonstrates that the variation of the ligand field splitting parameter, 10Dq, induced by the internal electric field comes mainly from the contributions of first shells of ions around the ${CrO_6}^{9-}$ unit. As a consequence, 10Dq in emerald is not influenced by the internal field, as the contribution from Be^{2+} first neighbors is practically compensated by that of Si^{4+} second neighbors. In contrast, in ruby the t_{2g} levels are shifted by the internal field 0.24 eV more than the e_g ones, so explaining the color shift in this gemstone in comparison with emerald. This result is shown to arise partially from the asymmetric form of the internal electrostatic potential along the C_3 axis in Al_2O_3.

DOI: 10.1103/PhysRevB.85.245118 PACS number(s): 71.55.−i, 71.15.Mb, 78.40.−q, 91.60.Mk

I. INTRODUCTION

The properties of oxides doped with Cr^{3+} ions, like ruby (Al_2O_3:Cr^{3+}), emerald ($Be_3Si_6Al_2O_{18}$:Cr^{3+}), or alexandrite ($BeAl_2O_4$:Cr^{3+}), have raised a great deal of interest.[1–22] Despite that in all oxides the Cr^{3+} impurity is surrounded by an octahedron of oxygen ligands, the color exhibited by gemstones like ruby and emerald, however, is not the same.[3,6] Historically, two main assumptions have been put forward for explaining such a difference. On one hand, some scientists have assumed that the mean Cr^{3+}-O^{2-} distance, R, is *not the same* for gemstones like ruby and emerald.[1,3,4,6,7,10,15,23] This idea relies on the fact that color is mainly determined by the energy of the ${}^4A_2(t_{2g}^3) \rightarrow {}^4T_2(t_{2g}^2\, e_g{}^1)$ spin allowed transition which is equal to the ligand field splitting parameter 10Dq.[24] Moreover, 10Dq is known to be very sensitive to hydrostatic pressures and thus to changes of the metal-ligand distance.[25,26]

By contrast, many other authors have suggested that unpaired electrons are not fully localized on the ${CrO_6}^{9-}$ complex as they are also present in the second and further coordination spheres, which are not the same in ruby and emerald.[2,27–29] According to this view the flow of electronic charge *outside* the ${CrO_6}^{9-}$ complex would be responsible for the different 10Dq value exhibited by gemstones like ruby and emerald.

Nevertheless, with regard to the first tentative explanation, accurate extended x-ray absorption fine structure (EXAFS) results carried out on ruby and emerald have proved that the mean Cr^{3+}-O^{2-} distance is *the same* within the experimental uncertainty of 1 pm.[9,13] Moreover, a significant presence of unpaired electrons beyond the first coordination sphere is not supported by electron nuclear double resonance (ENDOR) results obtained on *ionic* lattices like Al_2O_3 doped with Cr^{3+}.[30,31] *Ab initio* calculations carried out on transition metal impurities in ionic lattices are consistent with this view.[32,33]

Bearing in mind these facts, recent results on Cr^{3+}-doped different fluoride and oxide lattices have shown that the observed differences in absorption and emission spectra can *all* be understood by just considering the internal electric field, $\mathbf{E}_R(\mathbf{r})$, created by the rest of lattice ions upon the ${CrF_6}^{3-}$ or ${CrO_6}^{9-}$ complex, respectively, where active electrons are *confined*.[34] This internal field is generated by the corresponding electrostatic potential, $V_R(\mathbf{r})$, through $\mathbf{E}_R(\mathbf{r}) = -\nabla V_R(\mathbf{r})$. Obviously, covalency in the complex is influenced by such an internal field, although unpaired electrons are not flowing outside the complex. As insulating lattices like Al_2O_3, $Be_3Si_6Al_2O_{18}$, $BeAl_2O_4$ or $MgAl_2O_4$ are not isomorphous,[9,13,14,35–38] the *different shape* of $\mathbf{E}_R(\mathbf{r})$ has been shown to be greatly responsible for the different color due to substitutional Cr^{3+} impurities in such lattices.[11,12,17] Also the distinct optical and magnetic properties exhibited by transition-metal impurities in the normal perovskite $KMgF_3$ and in the *inverted* perovskite $LiBaF_3$ have been accounted for through the same mechanism.[32,34] Furthermore, it has been shown that $\mathbf{E}_R(\mathbf{r})$ plays a key role for understanding the local structure and the associated spectroscopic properties of Cu^{2+}- and Cr^{3+}-doped layered perovskites such as K_2AF_4 (A = Mg, Zn).[39]

Despite that the mere addition of the internal electric field $\mathbf{E}_R(\mathbf{r})$ to the ${CrO_6}^{9-}$ complex allows one to understand an important number of experimental facts corresponding to the Cr^{3+}-based gemstones, there is, however, a fundamental question which needs to be answered. As it has been pointed out, the internal electric field $\mathbf{E}_R(\mathbf{r})$ will modify the electronic density and covalency inside the $CrO_6{}^{9-}$ unit provided $V_R(\mathbf{r})$ is not a constant on the whole complex region. This conclusion follows directly from the Hohenberg-Kohn theorem.[40] Therefore, it is of fundamental importance to clarify whether such changes of electronic density are or are not *directly* related to the changes in 10Dq which are in turn responsible for the color shift. This work is addressed to shed light on this relevant matter.

For achieving this goal, we have first explored two representative gemstones as ruby and emerald by means of *ab initio* calculations. Aside from deriving the equilibrium Cr^{3+}-O^{2-} distances and the 10Dq value for both gemstones, particular attention is paid to look into the actual changes of electronic levels and the electronic density induced by $V_R(\mathbf{r})$. Bearing these results in mind, we investigate in a further step a model system where $V_R(\mathbf{r})$ keeps the cubic symmetry, thus making the analysis of results easier than for ruby or emerald where the local symmetry is C_3 and D_3, respectively.

This work is arranged as follows. As the present study is based on electron localization, the main facts supporting its validity are briefly reviewed in Sec. II. Relevant details of the employed *ab initio* methods are given in Sec. III. In Sec. IV the changes in electronic density due to the internal field $\mathbf{E}_R(\mathbf{r})$ for ruby and emerald are quantified. Section V is addressed to *quantify* the shift in 10Dq parameter directly associated with electronic density changes in the case of the model system. Some final remarks are presented in the last section.

II. ELECTRON LOCALIZATION

It is well known that the crystal field spectra of pure compounds like Cr_2O_3 or $KNiF_3$ look rather similar to those observed for Al_2O_3:Cr^{3+} or $KMgF_3$:Ni^{2+}.[2,24,26] This fact strongly supports that in all these systems active electrons are essentially localized in the $MX_6{}^{q-}$ complex ($M = Cr^{3+}, Ni^{2+}$) formed with the six X ligands (X = O, F). This conclusion is consistent with a general view by W. Kohn stressing that electron localization in the ground state is the fingerprint of every insulating material.[41–43]

Relevant experimental information on the degree of localization for impurities in insulating lattices is obtained from the ENDOR technique. For instance, in $KMgF_3$:Mn^{2+}, in addition to the average hyperfine constant for ligands $A_s(1)$, the ENDOR technique allows one to measure the corresponding constant $A_s(2)$ for the nearest F^- ions lying *outside* the $MnF_6{}^{4-}$ complex.[44] The values $A_s(1) = 54$ MHz and $A_s(2) = 0.64$ MHz thus support that active electrons are basically localized on the $MnF_6{}^{4-}$ unit. In the case of systems like Al_2O_3:Cr^{3+} there is no hyperfine interaction with ligands because the nuclear spin of the ^{16}O isotope is zero. However, the hyperfine interaction with the closest aluminum ions has been measured by ENDOR, obtaining an isotropic hyperfine constant $A_s(Al)$ at around 2 MHz.[30] Bearing in mind that an electron placed on the 3s orbital of free aluminum leads to a hyperfine constant A_s^0 = 3920 MHz,[45] the ratio $A_s(Al)/A_s^0$ implies that *only* a charge of the order of $5 \times 10^{-4}e$ has been transferred from the $CrO_6{}^{9-}$ unit to a close aluminum ion. ENDOR results on $MgAl_2O_4$:Cr^{3+},[31] or $RbCdF_3$:Cr^{3+} (Ref. 46) also show that the charge of active electrons is essentially confined in the complex formed by the impurity and its six nearest neighbors. A similar conclusion has been obtained from *ab initio* calculations carried out on big clusters where a $CrF_6{}^{3-}$ unit is embedded.[33]

III. COMPUTATIONAL DETAILS

In a first step, periodic *ab initio* calculations based on the density functional theory (DFT) have been carried out on ruby and emerald in order to obtain the equilibrium geometries around the Cr^{3+} impurities in both gemstones as well as values of the charges of the lattice ions. Calculations were performed with the CRYSTAL09 package that employs localized Gaussian basis sets to represent the Bloch orbitals.[47] All ions have been described by all-electron basis sets of reasonably high quality (5–11G for Be, 8–411G* for O, 85–11G for A1, 88–31G* for Si, and 86–411G** for Cr) taken from the CRYSTAL data base.[48] In the case of emerald we have used the hexagonal cell of $Be_3Si_6Al_2O_{18}$ with 58 ions, where the Cr^{3+} replaces an Al^{3+} ion of the lattice, while for ruby we used a 2 × 2 × 2 supercell with 80 atoms. We have treated the exchange and correlation of the electrons through the B1WC hybrid functional[49] that allows geometry and band gaps to be obtained with great accuracy and reliability not requiring the input of any semiempirical parameter by the user. For checking the reliability of the employed method the equilibrium geometries of pure Al_2O_3 and $Be_3Si_6Al_2O_{18}$ lattices have also been calculated.

In a second step, molecular DFT calculations have been carried out on $CrO_6{}^{9-}$ complexes either isolated or merely subject to the electric field $\mathbf{E}_R(\mathbf{r})$ generated by infinite point charges from the rest of the lattice. In all these cases the Cr^{3+}-O^{2-} distances correspond to the actual values for ruby and emerald. As it has been discussed in the previous section, the great localization of the electrons of the impurity makes that this simple $CrO_6{}^{9-}$ unit, but subject to the electric field $\mathbf{E}_R(\mathbf{r})$, it is enough to unveil the microscopic origin of the different optical properties displayed by Cr^{3+} in a series of oxides or fluorides.[11,12,17,34] Calculations have been performed by means of the ADF 2010.02 code.[50] The generalized gradient approximation (GGA) exchange-correlation energy was computed according to the Perdew-Wang-91 functional.[51] The core electrons (1s-3p for Cr and 1s for O) were kept frozen. Chromium ion was described through the basis sets of TZP quality [triple-ξ Slater-type orbital (STO) plus one polarization function], whereas a DZP basis set (double-ξ STO plus one polarization function) was used for oxygen ions. It has been reported in previous works[11,12,52] that in order to correctly represent the metal-ligand covalence in a cluster model it is necessary to use a smaller basis set size in the ligands than in the metal. For being sure about the reliability of our main conclusions, calculations with other basis sets and functionals have also been performed. As a salient feature the *main effect* introduced by $\mathbf{E}_R(\mathbf{r})$ on 10Dq is *always* found for every employed basis set or exchange-correlation functional. It is worth noting that calculated properties are found to be less dependent on the basis set using DFT than traditional methods based on the Hartree-Fock description.[53,54] 10Dq has always been calculated following the average of configuration procedure given in Ref. 55. The center of gravity of the small splitting undergone by the t_{2g} orbital under the trigonal site symmetry has been taken into account when deriving 10Dq.

In particular, assuming that 10Dq $\propto R^{-n}$, an exponent $n = 4.2$ has been found by means of these calculations. This figure is not far from the value $n = 4.5$ measured experimentally for ruby under hydrostatic pressure.[5] The electrostatic potential $V_R(\mathbf{r})$ coming from all ions of Al_2O_3 or $Be_3Si_6Al_2O_{18}$ crystals lying outside the $CrO_6{}^{9-}$ unit has been calculated by means of the Ewald method, following the procedure described in Ref. 56. The nominal ionic charges were employed in these calculations since our periodic calculations performed on Al_2O_3 and $Be_3Si_6Al_2O_{18}$ lattices have demonstrated that the total charges on oxygen, aluminum, beryllium, and silicon ions are practically equal to $-2e$, $+3e$, $+2e$, and $+4e$ (e = proton charge), respectively, pointing out that bonding is highly ionic indeed. A similar conclusion was previously reached by Sousa *et al.* in their study of Al_2O_3.[57]

IV. RESULTS FOR RUBY AND EMERALD

A. Ruby

The structure of the Al_2O_3 host lattice[9,36] is depicted on Fig. 1. A given Al^{3+} cation is surrounded by six O^{2-} anions, three at a *short* distance $R_s = 1.857$ Å and the rest lying further at $R_l = 1.969$ Å. The local symmetry is C_3. Along the C_3 axis there are two Al^{3+} ions neighbors of a given aluminum ion. One called Al_s^{3+} is located at 2.65 Å, while the other called Al_l^{3+} is placed much further at 3.80 Å. In the plane perpendicular to the C_3 axis there are three Al^{3+} ions lying at 2.79 Å. Such ions are called $Al_\perp^{3+}$ in Fig. 1.

The formation of ruby implies the $Al^{3+} \rightarrow Cr^{3+}$ substitution. Due to the different ionic radius of Al^{3+} and Cr^{3+}, this replacement is likely to modify the values of both R_s and R_l distances. The next section is focused on the actual R_s and R_l values when an Al^{3+} ion is replaced by Cr^{3+}, as they are important for a right interpretation of optical data of ruby.

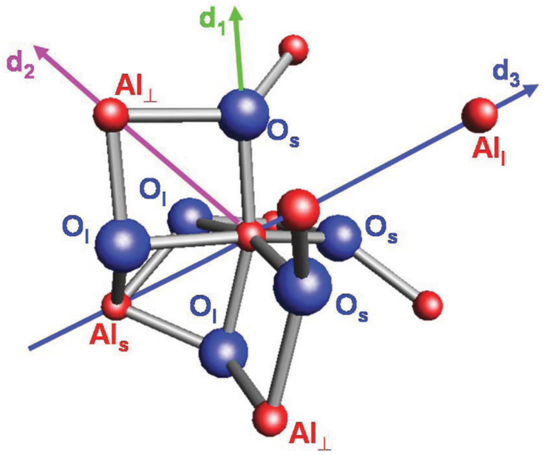

FIG. 1. (Color online) Local structure of corundum Al_2O_3 around an Al^{3+} ion with a C_3 symmetry. A given Al^{3+} cation is surrounded by six O^{2-} anions, three O_s at a *short* distance $R_s = 1.857$ Å and three O_s lying further at $R_l = 1.969$ Å. Along the C_3 axis there are two Al^{3+} ions neighbors of a given aluminum ion, one called Al_s^{3+} is located at 2.65 Å while the other called Al_l^{3+} is placed much further at 3.80 Å. In the plane perpendicular to the C_3 axis there are three $Al_\perp^{3+}$ ions lying at 2.79 Å.

TABLE I. Values of R_s and R_l distances (in angstroms) obtained in this work by means of periodic calculations for pure Al_2O_3. The values are compared to experimental data,[9,36] as well as to those previously calculated by Duan *et al.*[58] and Mazurenko *et al.*[59]

	Present work	Duan *et al.*	Mazurenko *et al.*	Experimental
R_s (Å)	1.868	1.839	1.85	1.857
R_l (Å)	1.976	1.969	1.98	1.969

1. *Local structure in ruby*

As a first step we have derived by means of periodic calculations the R_s and R_l values corresponding to the pure Al_2O_3 lattice. As shown in Table I the figures $R_s = 1.868$ Å and $R_l = 1.976$ Å are close to those previously obtained by Douan[58] and coincident within 1 pm with the experimental values $R_s = 1.857$ Å and $R_l = 1.969$ Å.[9,36]

The calculated equilibrium R_s and R_l distances corresponding to ruby are given in Table II where they are compared to the experimental EXAFS values obtained by Gaudry *et al.*,[9] as well as to figures derived in previous calculations. Values found in the present calculations are reasonably close to the experimental figures $R_s = 1.92 \pm 0.01$ Å and $R_l = 2.01 \pm 0.01$ Å and support that the mean Cr^{3+}-O^{2-} distance in ruby is $R_{av} = 1.97$ Å, which is thus identical to that measured for emerald.[13] It can also be seen in Table I that the metal-ligand distance values obtained in our calculations are very similar to those computed by other authors on the same 80-atom supercell but using different. However, unlike with previous calculations, all our calculations have been made using all-electron basis functions and hybrid functionals.

2. *Effect of the internal electric field on 10Dq*

The form of the electrostatic potential due to the rest of the lattice ions on the $CrO_6{}^{9-}$ complex $V_R(\mathbf{r})$ for three particular directions in ruby is depicted in Fig. 2. So, the changes of $V_R(\mathbf{r})$ along the O_s–Cr–O_l path (direction d_1), the diagonal joining the central Cr^{3+} impurity, one $Al_\perp^{3+}$ cation (direction d_2), and finally the C_3 axis (direction d_3) are all shown in Fig. 2.

As portrayed in Fig. 2, there is an electric field directed along the trigonal axis at the chromium site, a fact consistent with the C_3 local symmetry. Figure 2 also indicates that if unpaired electrons would be rigorously placed at the position of the chromium nucleus, its energy would experience a decrease of about -54 eV due to the action of $(-e)V_R(0)$. However, if the unpaired electronic density spreads on the $CrO_6{}^{9-}$ complex, $V_R(\mathbf{r})$ changes significantly in that region, as shown in Fig. 2. For instance, if $\mathbf{r}$ is varied along direction d_3, then $(-e)V_R(\mathbf{r}) = -85$ eV when $|\mathbf{r}| = 2$ Å and the electron is close to $Al_s{}^{3+}$, while $(-e)V_R(\mathbf{r}) = -45$ eV when it is at the same distance but in the *opposite* direction.

As shown in Fig. 3, the energy decrease induced by $(-e)V_R(\mathbf{r})$ is *different* for t_{2g} and e_g antibonding orbitals. In fact, while the center of the gravity of e_g levels moves downward by 52.22 eV, this figure is slightly higher (52.48 eV) for the case of t_{2g} levels, such as depicted in Fig. 3. This difference, though tiny, produces an increase in the 10Dq value. Indeed, if 10Dq is calculated for the isolated $CrO_6{}^{9-}$ complex at the right equilibrium geometry in ruby but ignoring the effects of

TABLE II. Values of Cr^{3+}-O^{2-} distances calculated by means of periodic calculations using an 80-atom supercell for Al_2O_3:Cr^{3+}. The R_l and R_s distances are compared to those measured by EXAFS (Ref. 9) and those derived by Duan *et al.*[58] and Gaudry *et al.*[9] through LDA Carr-Parinello methods, Mazurenko *et al.*[59] with a LDA + U tight-binding linear-muffin-tin method, and Watanabe *et al.*[18] with a GGA calculation.

	Calculated					
	Present work	Duan *et al.*	Gaudry *et al.*	Mazurenko *et al.*	Watanabe *et al.*	Experimental
R_s (Å)	1.942	1.918	1.95	1.93	1.922	1.92
R_l (Å)	1.997	2.018	2.00	1.99	1.986	2.01

$V_R(\mathbf{r})$, a value of 10Dq = 2.00 eV is obtained (Fig. 3), which is smaller than the experimental figure 10Dq = 2.24 eV.[3,6] Nevertheless, as shown in Fig. 3, the action of $(-e)V_R(\mathbf{r})$ on the $CrO_6{}^{9-}$ complex produces an increase of 10Dq of 0.24 eV that although small (12%), shifts the color of ruby from green to red. This conclusion is thus fully consistent with the results of a previous study.[11] Supporting this view a calculation carried out on a bigger $CrO_6Al_7{}^{9+}$ cluster including the electric field due to the rest of the ions of the Al_2O_3 lattice gives a value of 10Dq = 2.18 eV.

3. *Changes of electronic density due to the internal electric field*

The variations of charge distribution in the t_{2g} and e_g antibonding orbitals induced by the internal field of ruby upon the $CrO_6{}^{9-}$ unit are displayed in Table III. Results given in this table correspond to the ${}^4A_2(t_{2g}^3)$ ground state at the experimental equilibrium geometry of the $CrO_6{}^{9-}$ complex in ruby. In that state t_{2g} levels are half filled while the two e_g levels are unoccupied. Very close results to those reported in Table III are obtained for the average $t_{2g}^{3/5}e_g^{2/5}$ configuration.

The values gathered in Table III show that the internal electric field $\mathbf{E}_R(\mathbf{r})$ in ruby does *not* produce *drastic* changes on the electronic density for both t_{2g} and e_g antibonding levels. Indeed, the changes on the 3*d*(Cr) charge induced by the addition of $\mathbf{E}_R(\mathbf{r})$ are smaller than 4% for the two kinds of levels.

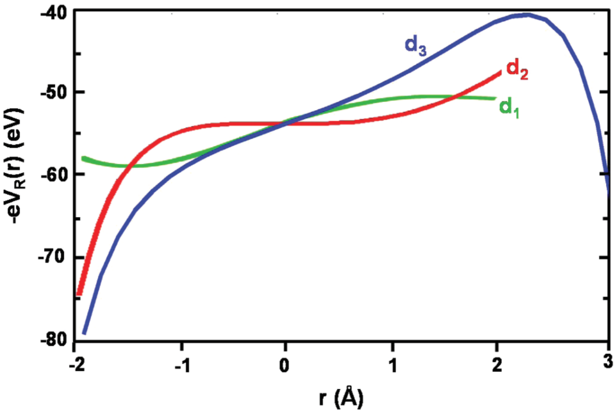

FIG. 2. (Color online) Potential energy on an electron, $(-e)V_R(\mathbf{r})$, due to the internal electric potential, $V_R(\mathbf{r})$, produced by the rest of the lattice ions of ruby on the CrO_6^{9-} complex. Energy is depicted along the O_s-Cr-O_l path (direction d_1), the diagonal joining the central Cr^{3+} impurity, and one $Al_{\perp}^{3+}$ cation (direction d_2) and the C_3 axis (direction d_3).

It can be noticed that in the *antibonding* e_g level the unpaired electron spends more time on O_s than on O_l oxygens. As the opposite happens for the corresponding bonding orbital which is fully occupied, this implies that there is a net flow of electronic charge going from O_s to O_l. This fact, similar to that discussed in $LiBaF_3$:Mn^{2+},[32] is consistent with the closeness of $Al_s{}^{3+}$ to the three O_l ligands (Fig. 1) and the form of $(-e)V_R(\mathbf{r})$ along the d_1 direction, such as it is shown in Fig. 2.

B. Emerald

1. *Local structure in emerald*

The structure of beryl ($Be_3Si_6Al_2O_{18}$) around an Al^{3+} ion is shown in Fig. 4.[13,37,38] The local symmetry is D_3, higher than in ruby, and all nearest O^{2-} anions lie at the same distance R = 1.903 Å, as shown in Table IV.Thus, this value is only 0.01 Å smaller than the average Al^{3+}-O^{2-} distance measured in Al_2O_3.

Results on the equilibrium geometry of beryl derived through periodic calculations are also collected in Table IV together with previous data obtained by Gaudry *et al.*[13] It can be noticed that all calculated R values gathered in Table IV are coincident with the experimental values within 0.4%. Similarly the experimental distances between an Al^{3+} ion and the three nearest Be^{2+} ions (2.66 Å) and the six closest Si^{4+} ions (3.26 Å) are reasonably reproduced by the calculations.

The replacement of an Al^{3+} by a Cr^{3+} impurity induces, as expected, a slightly outward relaxation, such as shown in Table V. The Cr^{3+}-O^{2-} distance derived by the present calculations (R = 1.968 Å) is coincident within 0.4% with

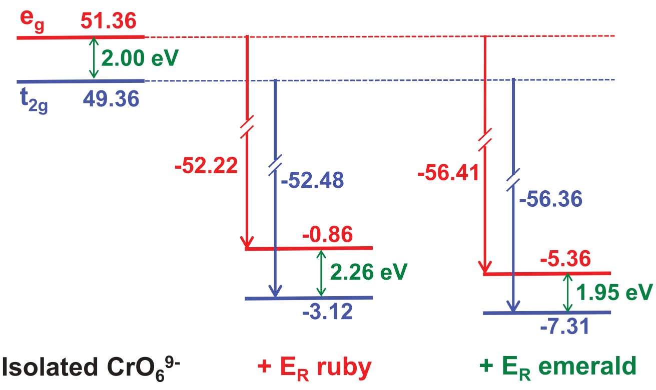

FIG. 3. (Color online) Scheme depicting the energy decrease induced by the $(-e)V_R(\mathbf{r})$ contribution for t_{2g} and e_g antibonding orbitals in ruby and emerald.

TABLE III. Mulliken populations (in percent) for antibonding e_g (first row) and t_{2g} (second row) levels of ruby derived from the present calculations for the ${}^4A_2(t_{2g}^3)$ ground state of a CrO_6^{9-} complex at the experimental equilibrium geometry. Results obtained for the isolated CrO_6^{9-} complex are compared with those derived taking into account the internal field $\mathbf{E}_R(\mathbf{r})$. Only the electronic charge lying on the $3d$ orbitals of chromium as well as that on $2p$ and $2s$ orbitals of three $\mathrm{O_l}$ and three $\mathrm{O_s}$ ligand ions is given. Due to the C_3 symmetry, the values given in this table mean an average value of three orbitals emerging from t_{2g} under strict cubic symmetry. Note that in ${}^4A_2(t_{2g}^3)$ ground state the antibonding e_g levels are unoccupied while they are partially occupied in the excited ${}^4T_2(t_{2g}^2\, e_g^1)$ state placed an energy 10Dq above the ground state.[24]

	Cr($3d$)	$2p(\mathrm{O_l})$	$2p(\mathrm{O_s})$	$2s(\mathrm{O_l})$	$2s(\mathrm{O_s})$
Isolated CrO_6^{9-}	77.62	11.00	8.32	1.12	1.44
	86.00	4.61	7.86	–	–
With $\mathbf{E}_R(\mathbf{r})$	76.06	10.41	11.82	0.83	1.40
	89.40	3.15	6.05	–	–

the experimental value reported by Gaudry *et al.*[13] and is thus essentially coincident with the average $\mathrm{Cr^{3+}}$-$\mathrm{O^{2-}}$ distance determined for ruby (Table II).

2. *Influence of the internal electric field in emerald*

The form of $(-e)V_R(\mathbf{r})$ energy for some particular directions in emerald is depicted in Fig. 5, where d_1, d_2, d_3, and d_4 directions correspond, respectively, to a O-Cr-O path joining two opposite oxygens, a C_2 axis joining $\mathrm{Cr^{3+}}$ with a close $\mathrm{Be^{2+}}$, and the C_3 axis and a path bisecting a O-Cr-O angle involving two adjacent oxygen ions which does not intersect a close $\mathrm{Be^{2+}}$ ion (Fig. 4). As it can be seen in Fig. 5, there is no electric field at the chromium site, a result consistent with the D_3 symmetry for emerald. Similarly to the case of ruby, $(-e)V_R(0) \approx -54$ eV. Nevertheless, the values of $(-e)|V_R(\mathbf{r}) - V_R(0)|$ for $|\mathbf{r}| \leqslant 2$ Å are, in general, smaller than those found for ruby (Fig. 2), although $-(e)V_R(\mathbf{r}) \approx -70$ eV when we move along the d_2 direction approaching the $\mathrm{Be^{2+}}$ ion.

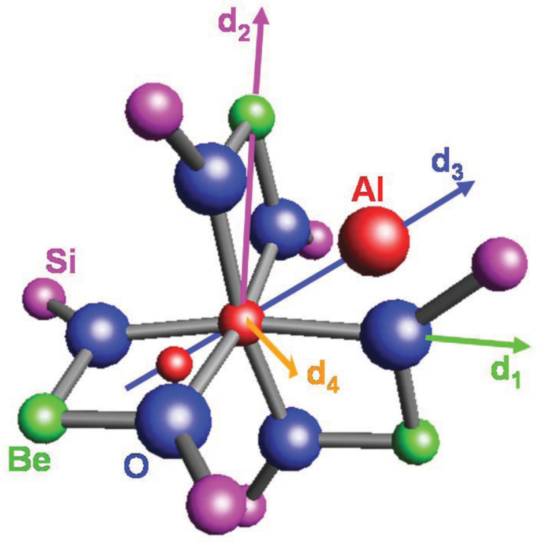

FIG. 4. (Color online) Local structure of beryl ($\mathrm{Be_3Si_6Al_2O_{18}}$) around an $\mathrm{Al^{3+}}$ ion with a D_3 symmetry. All nearest $\mathrm{O^{2-}}$ anions lie at the same distance $R = 1.903$ Å.

TABLE IV. Structural parameters (all in angstrom) of pure beryl ($\mathrm{Be_3Si_6Al_2O_{18}}$) derived from the present periodic calculations. Aside from the lattice parameters a and c, the distances between an $\mathrm{Al^{3+}}$ ion and its nearest $\mathrm{O^{2-}}$, $\mathrm{Be^{2+}}$, and $\mathrm{Si^{4+}}$ ions are reported. These values are compared to experimental figures derived by Gibbs *et al.*[37] as well as to the values of Al-O, Al-Be, and Al-Si distances obtained by Gaudry *et al.*[13] through periodic Carr-Parinello calculations.

	Present work	Gaudry *et al.*	Experimental
a	9.220	–	9.212
c	9.221	–	9.187
Al-O	1.904	1.90	1.903
Al-Be	2.662	2.66	2.66
Al-Si	3.283	3.26	3.26

The influence of $V_R(\mathbf{r})$ upon the 10Dq value in emerald is shown in Fig. 3 where it is compared to the results found for ruby. In can be noticed that, in the absence of the electrostatic potential due to the rest of the lattice ions on the $\mathrm{CrO_6}^{9-}$ complex, 10Dq would be the same for ruby and emerald. However, the changes in 10Dq due to $V_R(\mathbf{r})$ are very different in both gemstones, as shown in Fig. 3. In the case of emerald $V_R(\mathbf{r})$ induces a decrease of 56.413 eV and 56.357 eV on the energy of antibonding e_g and t_{2g} levels, respectively. Therefore, this implies only a *tiny* reduction of 0.05 eV on the 10Dq value calculated for the $\mathrm{CrO_6}^{9-}$ complex *in vacuo* and thus a final 10Dq value equal to 1.95 eV. This value can be compared with the experimental figure for emerald, 10Dq = 2.00 eV.[3,6]

We have also verified that the changes of electronic density induced by the internal electric field are certainly smaller for emerald than for ruby. For instance, the average $3d$(Cr) population for the three t_{2g} levels is found to vary by 0.15% due to the addition of the internal electric field.

V. STUDY OF A MODEL SYSTEM WITH CUBIC SYMMETRY

A. Description of the model

A central question in this study is to determine the influence of electronic density changes induced by $\mathbf{E}_R(\mathbf{r})$ on the *final* 10Dq value. This relevant matter has been explored in the model system described in Fig. 6. In that system an octahedral

TABLE V. Values of Al-O, Al-Be, and Al-Si distances (all in angstroms) derived from the present periodic calculations for emerald ($\mathrm{Be_3Si_6Al_2O_{18}{:}Cr^{3+}}$) and those previously obtained by Gaudry *et al.*[13] by means of periodic Carr-Parinello calculations. The value of the Cr-O distance measured by EXAFS (Ref. 13) is also included for comparison.

	Present work	Gaudry *et al.*	Experimental
Cr-O	1.968	1.99	1.97 ± 0.005
Cr-Be	2.695	2.70	–
Cr-Si	3.306	3.31	–

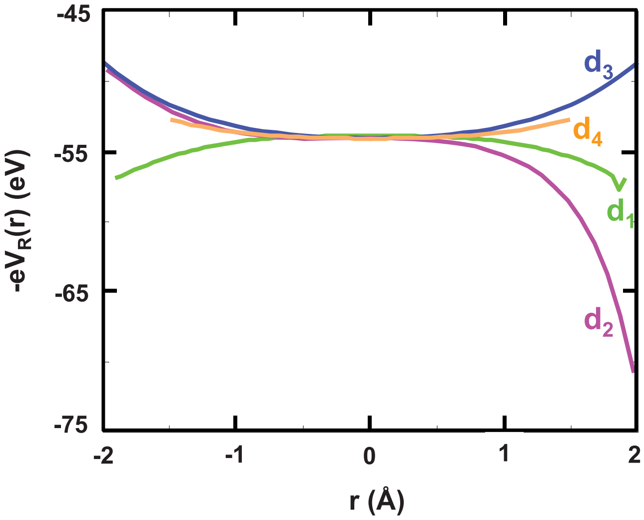

FIG. 5. (Color online) Potential energy $(-e)V_R(\mathbf{r})$ for emerald. Energy is depicted along d_1, d_2, d_3, and d_4 directions corresponding, respectively, to a O—Cr—O path joining two opposite oxygens, a C_2 axis joining Cr^{3+} with a close Be^{2+}, the C_3 axis, and a path bisecting a O—Cr—O angle involving two adjacent oxygens which does not intersect a close Be^{2+} ion (Fig. 4).

$\mathrm{CrO}_6{}^{9-}$ complex is surrounded by six identical *point charges* at the same distance R_q from the chromium and placed along the three C_4 axes of the octahedron. In this model system such point charges create the internal electric field on the $\mathrm{CrO}_6{}^{9-}$ unit but the octahedral symmetry is preserved. Particular attention has been paid to explore the variation of 10Dq as a function of the charge Q of the *external* point ion.

Although upon the addition of $V_R(\mathbf{r})$ the octahedral symmetry is kept, it modifies, however, the form of orbitals and its associated energy. Therefore the energy of a given orbital ε_n can be written as

$$\varepsilon_n = \varepsilon_n^0 + \varepsilon_n^1 + \varepsilon_n^2 + \cdots, \tag{1}$$

$$\varepsilon_n^1 = \langle \phi_n^0 | (-e) V_R | \phi_n^0 \rangle; \quad \varepsilon_n^2 = \sum_{n' \neq n} \frac{\left| \langle \phi_{n'}^0 | (-e) V_R | \phi_n^0 \rangle \right|^2}{\varepsilon_n^0 - \varepsilon_{n'}^0}. \tag{2}$$

Here ϕ_n^0 and ε_n^0 mean the wave function and energy, respectively, corresponding to the n orbital of the complex in the *absence* of the internal electric field. It is worth noting now that if $V_R(\mathbf{r})$ depends linearly on Q, then according to Eqs. (1) and (2), ε_n^1 and ε_n^2 *scale* like Q and Q^2, respectively.

Similarly to what is written in Eq. (1), the changes in 10Dq due to $V_R(\mathbf{r})$ can shortly be written as

$$10\mathrm{Dq}(Q) = 10\mathrm{Dq}(0) + \Delta_1 + \Delta_2 + \cdots, \tag{3}$$

where 10Dq(0) corresponds to the isolated complex, while Δ_1 and Δ_2 depend on Q and Q^2, respectively. It should be noticed now that Δ_1 reflects the 10Dq variation in first-order perturbation, which is derived using the *frozen* wave functions corresponding to $\mathbf{E}_R(\mathbf{r}) = 0$. By contrast, the correction called Δ_2 does reflect the change of electronic density induced by the internal electric field.

In an *isolated* transition metal complex the *antibonding* t_{2g} and e_g levels have the form[24]

$$|t_{2g}; r\rangle = \alpha_t |d(t_{2g}); r\rangle - \beta_{p\pi} |\chi_{p\pi}; r\rangle \quad (r = xy, xz, yz), \tag{4}$$

$$|e_g; r\rangle = \alpha_e |d(e_g); r\rangle - \beta_{p\sigma} |\chi_{p\sigma}; r\rangle - \beta_s |\chi_s; r\rangle$$
$$(r = x^2 - y^2, 3z^2 - r^2). \tag{5}$$

In Eq. (4) the first term on the right describes a pure d wave function transforming like xy, xz, or yz, while the second term means a suitable linear combination of atomic orbitals (LCAO) involving p_σ valence orbitals of six ligands. The coefficients α_t^2 and $\beta_{p\pi}^2$ thus reflect the probability of finding the electron on the central cation and on ligands, respectively. In the case of the antibonding e_g orbital, symmetry allows an admixture with valence $2p_\sigma$ and $2s$ orbitals if the ligands are oxygens.[24]

Let us now see what the changes of both t_{2g} and e_g levels due to the *addition* of an internal field which keeps the cubic symmetry are. According to Eq. (2), if $V_R(\mathbf{r})$ also exhibits cubic symmetry, such orbitals can be mixed only with orbitals of the same label. So, the antibonding t_{2g} level can be mixed with the bonding counterpart called t_{2g}^b, giving rise to changes in $\beta_{p\pi}$. Similarly, the antibonding e_g level for the isolated complex mixes with the mainly $2p_\sigma$ level called e_g^b, as well as with the mainly $2s$ level denoted as e_g^s. This admixture leads to changes of $\beta_{p\sigma}$ and β_s quantities when a nonconstant $V_R(\mathbf{r})$ potential on the complex is switched on.

Let us denote by $\beta_{p\sigma}(\mathbf{E})$, $\beta_s(\mathbf{E})$, or $\beta_{p\pi}(\mathbf{E})$ the molecular orbital coefficients associated with a given $\mathbf{E}_R(\mathbf{r})$. Obviously, if there is no electric field $\beta_{p\sigma}(0) \equiv \beta_{p\sigma}$, $\beta_s(0) \equiv \beta_s$ and $\beta_{p\pi}(\mathbf{0}) \equiv \beta_{p\pi}$. Using second-order perturbation theory, the expression for Δ_2 turns out to be

$$\begin{aligned}\Delta_2 = {} & [\beta_{p\sigma}(\boldsymbol{E}) - \beta_{p\sigma}]^2 \left[\varepsilon(e_g) - \varepsilon\left(e_g^b\right)\right] \\ & + [\beta_s(\boldsymbol{E}) - \beta_s]^2 \left[\varepsilon(e_g) - \varepsilon\left(e_g^s\right)\right] \\ & + [\beta_{p\pi}(\boldsymbol{E}) - \beta_{p\pi}]^2 \left[\varepsilon(t_{2g}) - \varepsilon\left(t_{2g}^b\right)\right],\end{aligned} \tag{6}$$

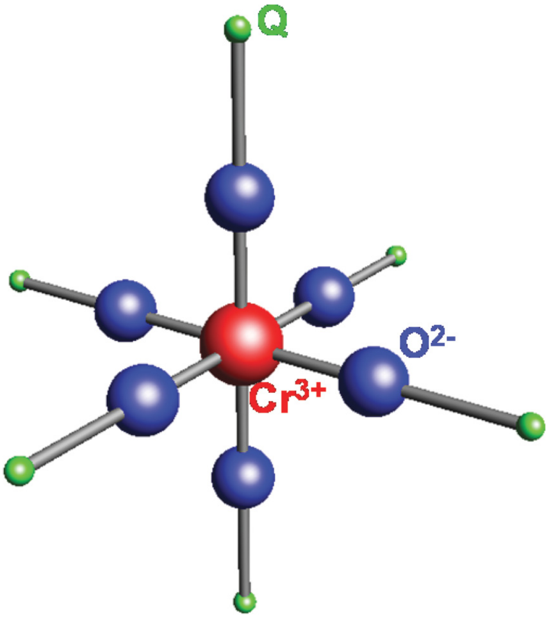

FIG. 6. (Color online) Model system formed by an octahedral CrO_6^{9-} complex surrounded by six identical point charges Q at the same distance R_q from the chromium ion and placed along the three C_4 axes of the octahedron.

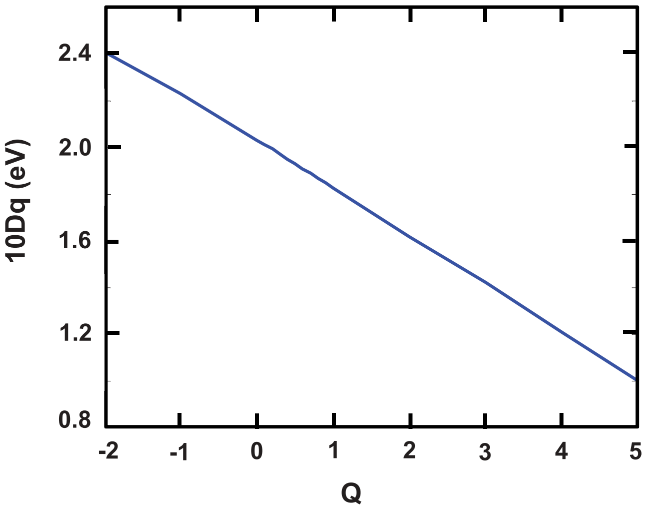

FIG. 7. (Color online) Calculated values of 10Dq as a function of the external charge Q for the model system. The external charges are placed at a distance $R_q = 4$ Å from the chromium ion.

where $\varepsilon(e_g)$, $\varepsilon(t_{2g})$, $\varepsilon(e_g^b)$, $\varepsilon(e_g^s)$, or $\varepsilon(t_{2g}^b)$ stand for orbital energies of the *isolated* complex. This expression allows one to estimate the value of Δ_2 associated with a given internal field from the values of $\beta_{p\sigma}(\mathbf{E})$, $\beta_s(\mathbf{E})$, or $\beta_{p\pi}(\mathbf{E})$ and the orbital energies of the isolated complex derived from *ab initio* calculations.

B. Results on the model system

Calculated values of 10Dq as a function of the external charge Q are portrayed in Fig. 7 where Q is varied in the range between $-2e$ and $5e$. It can be noticed that the dependence of the calculated 10Dq upon Q is essentially *linear*. Bearing in mind that the contributions Δ_1 and Δ_2 in Eq. (3) scale like Q and Q^2, respectively, the results displayed in Fig. 7 already suggest that the changes in electronic density play a minor role for understanding the variations undergone by 10Dq due to the presence of the internal field. In other words, the changes are primarily due to first-order effects [reflected in Eq. (2)], thus involving only the *frozen* wave functions of the isolated complex.

Seeking to reinforce this view, we have estimated the Δ_2 contribution by means of Eq. (6) and the values of $\beta_{p\sigma}(\mathbf{E})$, $\beta_s(\mathbf{E})$, $\beta_{p\pi}(\mathbf{E})$, and the involved excitations derived from the present calculations. In Table VI the values of 10Dq and the $\beta_{p\sigma}(\mathbf{E})$, $\beta_s(\mathbf{E})$, $\beta_{p\sigma}(\mathbf{E})$ parameters calculated for $Q = 3e$ are compared to those for the complex *in vacuo* ($Q = 0$). For estimating the second-order contribution Δ_2, we have used the values $\varepsilon(e_g) - \varepsilon(e_g^b) = 8.2$ eV, $\varepsilon(t_{2g}) - \varepsilon(t_{2g}^b) = 6.4$ eV, and $\varepsilon(e_g) - \varepsilon(e_g^s) = 21$ eV derived from the present calculations for $Q = 0$.

It can be remarked in Table VI that on passing from the complex *in vacuo* to $Q = 3e$, the value of 10Dq decreases by 0.6 eV, while Δ_2 is estimated to be *one order of magnitude* lower. Bearing in mind that 10Dq(Q) $-$ 10Dq(0) for $Q = 3e$ is four times bigger in the model system than for ruby, it is thus reasonable to accept that in all these cases the changes in 10Dq are governed by the Δ_1 contribution where only the *frozen* wave functions of the isolated complex are involved.

TABLE VI. Values of 10Dq (in electronvolts) and the covalency parameters $\alpha_e^2(\mathbf{E})$, $\alpha_t^2(\mathbf{E})$, $\beta_{p\sigma}^2(\mathbf{E})$, $\beta_{p\pi}^2(\mathbf{E})$, and $\beta_s^2(\mathbf{E})$ (in percent) calculated for the model system formed by the CrO_6^{9-} complex and six point charges Q keeping the octahedral symmetry. The results obtained for $Q = 3e$ are compared to those derived for the isolated complex ($Q = 0$). The value of the contribution to 10Dq called Δ_2 (in electronvolts) is estimated by means of Eq. (6) and the calculated values of $\beta_i^2(\mathbf{E})$ parameters.

	10Dq	α_e^2 (E)	α_t^2 (E)	$\beta_{p\sigma}^2$ (E)	$\beta_{p\pi}^2$ (E)	β_s^2 (E)	Δ_2
$Q = 0$	2.03	77.3	87.5	18.5	10.9	2.9	0
$Q = 3e$	1.42	82.0	86.0	10.7	13.3	5.0	0.08

On Fig. 8 the form of $(-e)V_R(\mathbf{r})$ along $\langle 100\rangle$ and $\langle 110\rangle$ directions is depicted. It can be noted that, as expected, when $\mathbf{r}$ is parallel to $\langle 100\rangle$ then $(-e)V_R(\mathbf{r}) < (-e)V_R(0)$ and thus the electrons which are close to ligands experience a *supplementary* electrostatic attraction. Let us now consider an $\mathrm{e_g}$ level where the electronic charge is lying mainly along $\langle 100\rangle$ directions. Therefore, if we designate by $|e_g^0\rangle$ the wave function of such a level for $Q = 0$, then, according to Fig. 8 the quantity $\langle e_g^0|(-e)V_R|e_g^0\rangle$ tends to *decrease* the energy of the e_g level. On the contrary, $(-e)V_R(\mathbf{r})$ along $\langle 110\rangle$ directions increases slightly when $|\mathbf{r}|$ does. This result is consistent with the form of an electrostatic potential $V_R(\mathbf{r})$ in cubic symmetry:[24]

$$V_R(\mathbf{r}) = A\left(x^4 + y + z^4 - \tfrac{3}{5}r^4\right) + \cdots. \tag{7}$$

As in the t_{2g} level, if the wave functions are pointing at $\langle 110\rangle$ directions, then the quantity $\langle t_{2g}^0|(-e)V_R|t_{2g}^0\rangle$ *increases* the energy of such a level. Therefore, in accordance with this reasoning, the electric field reflected in Fig. 8 tends to reduce the 10Dq value. This explains, albeit qualitatively, the results displayed in Table VI.

It is worth noting now that the addition of $V_R(\mathbf{r})$ increases the value of α_e^2 corresponding to the antibonding e_g level

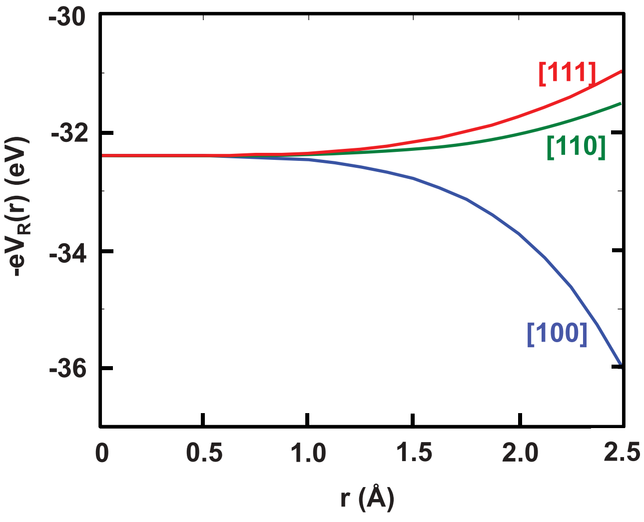

FIG. 8. (Color online) Form of $(-e)V_R(\mathbf{r})$ along $\langle 100\rangle$ and $\langle 110\rangle$ directions in the octahedral model system.

(Table VI), while the opposite happens for the fully occupied e_g^b level. This gives rise again to a *net* flow of the electronic charge from central ion to ligands consistent with the form of $(-e)V_R(\mathbf{r})$ along the $\langle 100\rangle$ directions depicted in Fig. 8.

Following the present analysis, if we rotate the four Q charges lying in the XY plane by an angle $\theta = 45°$ it can be expected that this new potential decreases the energy of the xy orbital while increasing that corresponding to the x^2-y^2 orbital. Despite that this new potential has a tetragonal symmetry, we have verified that it increases the separation between xy and x^2-y^2 orbitals and the 10Dq value.

C. Application to gemstones

The analysis carried out in the foregoing section strongly supports that the change in 10Dq in ruby is essentially *related neither to the polarization* of the chromium ion nor to the polarization change on ligands induced by the internal electric field. In fact, both phenomena do involve a change of electronic density, while we have shown that these effects play a secondary role for understanding the changes due to $\mathbf{E}_R(\mathbf{r})$. The present analysis points out that the changes in 10Dq arise from the different form of $V_R(\mathbf{r})$ along different directions *keeping* the electronic density of the isolated complex. In the case of ruby the form of $V_R(\mathbf{r})$ along d_2 and d_3 directions (Fig. 2) is *not symmetric* around $\mathbf{r} = 0$, and $(-e)\{V_R(\mathbf{r} - V_R(\mathbf{0})\} < 0$ when we approach a close aluminum ion. Bearing in mind that t_{2g} orbitals are lying mainly along such directions,[17] the action of $(-e)V_R(\mathbf{r})$ tends to decrease the energy of such orbitals. By contrast, the variation of $V_R(\mathbf{r})$ along metal-ligand directions is more symmetric and much softer than for d_2 and d_3 directions. Therefore, it can reasonably be expected that $V_R(\mathbf{r})$ induces a bigger decrease for t_{2g} orbitals than for e_g ones lying along metal-ligand directions. This explains albeit qualitatively the increase of 10Dq due to the internal field in the case of ruby (Fig. 3).

In the case of emerald (Fig. 5), the quantity $|V_R(\mathbf{r}) - V_R(\mathbf{0})|$ is in general smaller than that obtained for ruby. Nevertheless, it is comparable to that found for the model system (Fig. 8). Despite this fact the internal field only produces a little variation on 10Dq in the case of emerald. If we look at d_2, d_3, and d_4 directions where t_{2g} orbitals are lying, we see that the effect of $V_R(\mathbf{r})$ is *not homogeneous*. For instance, it tends to raise the orbital energy for d_3 and d_4 directions while when the electron approaches a close Be^{2+} such energy decreases. This suggests the existence of a compensation mechanism behind the actual 10Dq value for emerald.

For clarifying this matter we have calculated the 10Dq value of the emerald including in $V_R(\mathbf{r})$ *only* the electrostatic potential coming from the nearest Be^{2+} ions. In a second step we have also included in the calculation the electrostatic potential arising from the six nearest Si^{4+} ions. These results, gathered in Table VII, are compared to those obtained including in $V_R(\mathbf{r})$ all ions lying outside the CrO_6^{9-} complex. It can be noticed that if only the nearest Be^{2+} ions are considered when calculating $V_R(\mathbf{r})$, it leads to 10Dq = 2.20 eV, which is 10% higher than the value obtained for the isolated CrO_6^{9-} unit at $R = 1.97$ Å. By contrast, when the next shell involving six Si^{4+} ions at 3.31 Å from Cr^{3+} is also taken into account, then the value 10Dq = 1.93 eV is practically coincident with the figure 10Dq = 1.95 eV obtained including in $V_R(\mathbf{r})$ all ions lying outside the CrO_6^{9-} complex. On one hand, this fact stresses that the quantity $V_R(\mathbf{r}) - V_R(\mathbf{0})$ governing 10Dq mainly depends on the first shells around the complex. In other words, although all ions are contributing to $V_R(\mathbf{0})$, nevertheless $V_R(\mathbf{r}) - V_R(\mathbf{0})$ and Δ_1 are essentially reproduced considering *only* a few shells of ions around the complex.[32,60] On the other hand, it proves that the very small changes induced by $V_R(\mathbf{r})$ on the 10Dq value in emerald is the result of a practical *cancellation* of the contribution due to the three Be^{2+} ions at 2.66 Å by that coming from six Si^{4+} ions at 3.31 Å. This finding has some similarities with the near independence of 10Dq upon $V_R(\mathbf{r})$ in the case of perovskites like $KMgF_3$ doped with Mn^{2+} or Ni^{2+}.[32] In such a case this behavior comes from the cancellation of the contribution to 10Dq due to the first shell of eight K^+ ions by that of the second shell involving six Mg^{2+} ions. By contrast, a different situation holds for the *inverse* perovskite $LiBaF_3$ doped with divalent impurities where Δ_1 arises mainly from the first shell made by eight Ba^{2+} ions.[32]

TABLE VII. Calculated 10Dq values (in electronvolts) for the emerald with four different representations of $V_R(\mathbf{r})$: (a) $V_R(\mathbf{r}) = 0$ (isolated complex); (b) including only the first shell of three Be^{2+} ions lying outside the CrO_6^{9-} complex; (c) including the first and also the second shell composed by six Si^{4+} ions; and (d) including in $V_R(\mathbf{r})$ all ions lying outside the CrO_6^{9-} complex. In all cases the Cr^{3+}-O^{2-} distance is $R = 1.97$ Å.

System	10Dq
Isolated CrO_6^{9-} unit	2.007
CrO_6^{9-} + $3Be^{2+}$	2.200
CrO_6^{9-} + $3Be^{2+}$ + $6Si^{4+}$	1.933
CrO_6^{9-} + all lattice charges	1.951

VI. FINAL REMARKS

The present results stress the relevance of internal fields for a good understanding of optical and magnetic properties of transition-metal impurities in insulators. This situation thus has some connections with the interpretation of the quadrupole splitting on a given nucleus placed in a noncubic site, observed either in Mossbauer spectroscopy[61] or through magnetic resonance techniques.[62] Indeed, a right understanding of such splitting requires calculation of the quantities $(\partial^2 V/\partial x_i^2)_0$ at the nucleus site ($x_i = 0$), where $V(x_i)$ just means the electrostatic potential around the nucleus due to the rest of nuclei and the electronic charge.[63]

The results and analysis carried out in this work confirm that the different color exhibited by Cr^{3+} gemstones is due neither to differences in the mean Cr^{3+}-O^{2-} distance nor to the flow of unpaired electrons outside the CrO_6^{9-} unit. By contrast, the small changes in 10Dq and the color shift in the series of *ionic* oxides doped with Cr^{3+} can reasonably be understood considering only the CrO_6^{9-} unit and the internal field $\mathbf{E}_R(\mathbf{r})$ created by the rest of lattice ions upon the *localized* electrons. This result thus concurs with a previous study showing that the separation $\Delta(^4T_1; ^4T_2)$ between $^4T_2(t_{2g}^2 e_g^1)$ and $^4T_1(t_{2g}^2 e_g^1)$

states as well as the energy $E(^2E)$ of the $^2E(t_{2g}^3) \rightarrow {}^4A_2(t_{2g}^3)$ emission transition of Cr^{3+} in different lattices can be well accounted for on the same grounds.[34]

As a salient feature the present study demonstrates *quantitatively* that the modifications of electronic density due to the internal field do not play a relevant role for understanding the changes induced on the $^4A_2(t_{2g}^3) \rightarrow {}^4T_2(t_{2g}^2\, e_g^1)$ transition and thus the color of the gemstone. Therefore, although $\mathbf{E}_R(\mathbf{r})$ modifies the covalency in the CrO_6^{9-} unit, this small change is not the main factor responsible for the different 10Dq exhibited by ruby and emerald, a conclusion which is against previous assumptions.[11,64]

Although 10Dq can be understood by merely taking into account first-order effects induced by the internal field, this is no longer true for other quantities like $\Delta(^4T_1;\, ^4T_2)$, which are nearly independent of 10Dq. Indeed the variations of this quantity along the series of oxides or fluorides have been shown to reflect the changes induced by the internal field on the electronic density.[34]

It is worth noting now the similarities between the present problem and the static Jahn-Teller effect taking place, for instance, for d^9 ions under an *initial* coordination which is *perfectly* octahedral. In such cases the values of axial and equatorial metal-ligand distances of the *equilibrium* tetragonal geometry and the involved Jahn-Teller energy, E_{JT}, can also be understood only through the *frozen* wave functions corresponding to the initial high-symmetry configuration. By contrast, the barrier among equivalent distorted configurations partially depends on the electronic density change induced by the distortion.[65]

Despite the fact that all ions outside the CrO_6^{9-} unit contribute to the electrostatic potential at the chromium site $V_R(\mathbf{0})$, it has been emphasized through this work that the variations on 10Dq come from the quantity $V_R(\mathbf{r}) - V_R(\mathbf{0})$, which is essentially reproduced through the first shells of ions around the complex. A similar conclusion was reached in a previous study on the color shift along the series of $Al_{2-x}Cr_xO_3$ mixed crystals.[60]

Bearing in mind the present study, it is tempting to try to explain why the 10Dq value measured for MgO:Cr^{3+} (Ref. 66) is coincident with that of emerald. As the Mg^{2+}-O^{2-} distance in MgO is 2.10 Å, it is hard to accept that the Cr^{3+}-O^{2-} distance in MgO:Cr^{3+} is the same as in emerald. Work along this line is now underway.

ACKNOWLEDGMENTS

Support from the Spanish Ministerio de Ciencia y Tecnología under Project No. FIS2009-07083 is acknowledged.

---

[1] L. E. Orgel, Nature (London) **179**, 1348 (1957).

[2] D. Reinen, Struct. Bonding **6**, 30 (1969).

[3] K. Nassau, *The Physics and Chemistry of Colour* (John Wiley & Sons, New York, 1983).

[4] R. Reisfeld and C. K. Jørgensen, Struct. Bonding **69**, 63 (1988).

[5] S. J. Duclos, Y. K. Vohra, and A. L. Ruoff, Phys. Rev. B **41**, 5372 (1990).

[6] R. G. Burns, *Mineralogical Applications of Crystal Field Theory* (Cambridge University Press, Cambridge, 1993).

[7] J. Simmons and K. S. Potter, *Optical Materials* (Academic Press, New York, 2000).

[8] T. H. Yeom and S. H. Choh, J. Appl. Phys. **90**, 5946 (2001).

[9] E. Gaudry, A. Kiratisin, P. Sainctavit, C. Brouder, F. Mauri, A. Ramos, A. Rogalev, and J. Goulon, Phys. Rev. B **67**, 094108 (2003).

[10] V. S. Urusov and M. N. Taran, Phys. Chem. Miner. **39**, 17 (2012).

[11] J. M. Garcia-Lastra, M. T. Barriuso, J. A. Aramburu, and M. Moreno, Phys. Rev. B **72**, 113104 (2005).

[12] J. M. Garcia-Lastra, J. A. Aramburu, M. T. Barriuso, and M. Moreno, Phys. Rev. B **74**, 115118 (2006).

[13] E. Gaudry, D. Cabaret, C. Brouder, I. Letard, A. Rogalev, F. Wilhlem, N. Jaouen, and P. Sainctavit, Phys. Rev. B **76**, 094110 (2007).

[14] A. Juhin, G. Calas, D. Cabaret, L. Galoisy, and J.-L. Hazemann, Phys. Rev. B **76**, 054105 (2007).

[15] R. J. D. Tilley, *Defects in Solids* (John Wiley & Sons, New York, 2008).

[16] K. Krambrock, K. J. Guedes, and M. Pinheiro, Phys. Chem. Miner. **35**, 409 (2008).

[17] J. M. Garcia-Lastra, M. T. Barriuso, J. A. Aramburu, and M. Moreno, Phys. Rev. B **78**, 085117 (2008).

[18] S. Watanabe, T. Sasaki, R. Taniguchi, T. Ishii, and K. Ogasawara, Phys. Rev. B **79**, 075109 (2009).

[19] G. Cruciani, M. Ardit, M. Dondi, F. Matteucci, M. Blosi, M. Dalconi, and S. Albonetti, J. Phys. Chem. A **113**, 13772 (2009).

[20] F. Farges, Phys. Chem. Miner. **36**, 463 (2009).

[21] U. Halenius, G. B. Andreozzi, and H. Skogby, Am. Mineral. **95**, 456 (2010).

[22] B. D. Fahlman, *Materials Chemistry* (Springer, Dordrecht, 2011).

[23] M. Andrut, M. Wildner, and C. Z. Rudowicz, in *Optical Absorption Spectroscopy in Geosciences. Part II: Quantitative Aspects of Crystal Fields*, edited by A. Beran and E. Libowitzky, EMU Notes in Mineralogy, Vol. 6 (University Press, Budapest, 2004), p. 145.

[24] S. Sugano, Y. Tanabe, and H. Kamimura, in *Multiplets of Transition-Metal Ions in Crystals* (Academic Press, New York, 1970), p. 331.

[25] H. G. Drickamer and C. W. Frank, *Electronic Transitions and the High Pressure Chemistry of Solids* (Chapman Hall, London, 1973).

[26] M. Moreno, M. T. Barriuso, J. A. Aramburu, P. Garcia-Fernandez, and J. M. Garcia-Lastra, J. Phys. Condens. Matter **18**, R315 (2006).

[27] D. L. Wood, J. Ferguson, K. Knox, and J. F. Dillon, J. Chem. Phys. **39**, 890 (1963).

[28] D. Reinen, M. Atanasov, and S. L. Lee, Coord. Chem. Rev. **175**, 91 (1998).

[29] H. Thauern and R. Glaum, Inorg. Chem. **46**, 2057 (2007).

[30] N. Laurance, E. C. McIrvine, and J. Lambe, J. Phys. Chem. Solids **23**, 515 (1962).

[31] D. Bravo and R. Bottcher, J. Phys. Condens. Matter **4**, 7295 (1992).

[32] A. Trueba, J. M. García-Lastra, M. T. Barriuso, J. A. Aramburu, and M. Moreno, Phys. Rev. B **78**, 075108 (2008).

[33] J. M. García-Lastra, M. T. Barriuso, J. A. Aramburu, and M. Moreno, J. Phys. Condens. Matter **22**, 155502 (2010).

[34] A. Trueba, J. M. García-Lastra, P. Garcia-Fernandez, M. T. Barriuso, J. A. Aramburu, and M. Moreno, J. Phys. Chem. A **115**, 13399 (2011).

[35] R. C. Powell, *Physics of Solid State Laser Materials* (Springer, New York, 1998).

[36] R. W. G. Wyckoff, *Crystal Structures*, Vol. 1 (John Wiley & Sons, New York, 1963).

[37] G. V. Gibbs, D. W. Breck, and E. P. Meagher, Lithos **1**, 275 (1968).

[38] B. Morosin, Acta Crystallogr. B **28**, 1899 (1972).

[39] J. M. García-Lastra, J. A. Aramburu, M. T. Barriuso, and M. Moreno, Phys. Rev. Lett. **93**, 226402 (2004); Chem. Phys. Lett. **385**, 286 (2004).

[40] R. G. Parr and W. Yang, *Density-Functional Theory of Atoms and Molecules* (Oxford University Press, New York, 1989).

[41] W. Kohn, Phys. Rev. A **133**, 171 (1965).

[42] W. Kohn, Phys. Rev. Lett. **76**, 3168 (1996).

[43] R. Resta, J. Phys. Condens. Matter **14**, R625 (2002).

[44] R. K. Jeck and J. J. Krebs, Phys. Rev. B **5**, 1677 (1972).

[45] J. A. Weil, J. R. Bolton, and J. E. Werz, *Electron Paramagnetic Resonance* (Wiley, New York, 1994).

[46] P. Studzinski and J. M. Spaeth, Phys. Status Solidi B **136**, 735 (1986).

[47] R. Dovesi, R. Orlando, B. Civalleri, C. Roetti, V. R. Saunders, and C. M. Zicovich-Wilson, Kristallogr. **220**, 571 (2005).

[48] CRYSTAL basis sets, http://www.crystal.unito.it/Basis_Sets/Ptable.html.

[49] D. I. Bilc, R. Orlando, R. Shaltaf, G.-M. Rignanese, J. Iñiguez, and Ph. Ghosez, Phys. Rev. B **77**, 165107 (2008).

[50] G. te Velde, F. M. Bickelhaupt, E. J. Baerends, C. F. Guerra, S. J. A. van Gisbergen, J. G. Snijders, and T. Ziegler, J. Comput. Chem. **22**, 931 (2001).

[51] J. P. Perdew, in *Electronic Structure of Solids' 91*, edited by P. Ziesche and H. Eschrig (Akademie Verlag, Berlin, 1991), p. 11.

[52] J. A. Aramburu, J. M. García-Lastra, M. T. Barriuso, and M. Moreno, Int. J. Quantum Chem. **91**, 197 (2003).

[53] N. Lopez and F. J. Illas, J. Phys. Chem. B **102** 1430 (1998).

[54] M. T. Barriuso, J. A. Aramburu, and M. Moreno, J. Phys. Condens. Matter **11**, L525 (1999).

[55] M. Atanasov, C. A. Daul, and C. Rauzy, Chem. Phys. Lett. **367**, 737 (2003).

[56] J. A. Aramburu, M. Moreno, K. Doclo, C. Daul, and M. T. Barriuso, J. Chem. Phys. **110**, 1497 (1999).

[57] C. Sousa, C. de Graaf, and F. Illas, Phys. Rev. B **62**, 10013 (2000).

[58] W. Duan, G. Paiva, R. M. Wentzcovitch, and A. Fazzio, Phys. Rev. Lett. **81**, 3267 (1998).

[59] V. V. Mazurenko, A. N. Varaksin, V. G. Mazurenko, V. S. Kortov, and V. I. Anisimov, Physica B **344**, 385 (2004).

[60] J. M. García-Lastra, M. T. Barriuso, J. A. Aramburu, and M. Moreno, Phys. Rev. B **79**, 241106(R) (2009).

[61] A. Vertes, L. Korecz, and K. Burger, in *Mössbauer Spectroscopy* (Elsevier, Amsterdam, 1979), p. 40.

[62] A. Abragam and B. Bleaney, in *Electron Paramagnetic Resonance of Transition Ions* (Clarendon Press, Oxford, 1970), p. 414.

[63] P. Blaha, K. Schwarz, W. Faber, and J. Luitz, Hyperfine Interact. **126**, 389 (2000).

[64] N. Wiberg, A. F. Holleman, and E. Wiberg, in *Inorganic Chemistry* (Academic Press, San Diego, CA, 2001), p. 1198.

[65] P. García-Fernández, I. B. Bersuker, J. A. Aramburu, M. T. Barriuso, and M. Moreno, Phys. Rev. B **71**, 184117 (2005).

[66] S. Kück, L. Fornasiero, E. Heumann, E. Mix, G. Huber, T. Kärner, and A. Maaroos, Laser Phys. **10**, 411 (2000).